



OPEN ACCESS

EDITED BY

Francesca Zambon,
National Institute of Astrophysics
(INAF), Italy

REVIEWED BY

Stefano Bertone,
University of Maryland, United States
Yutong Jia,
Space Engineering University, China

*CORRESPONDENCE

Fei Li,
✉ fli@whu.edu.cn

RECEIVED 10 December 2025

REVISED 05 March 2026

ACCEPTED 09 March 2026

PUBLISHED 30 March 2026

CITATION

Chen Y, Ye M, Qiu D and Li F (2026)
High-resolution accessibility and energy
cost assessment of 31 priority
permanently shadowed regions at the
lunar south pole.

Front. Astron. Space Sci. 13:1764826.
doi: 10.3389/fspas.2026.1764826

COPYRIGHT

© 2026 Chen, Ye, Qiu and Li. This is an
open-access article distributed under
the terms of the [Creative Commons
Attribution License \(CC BY\)](https://creativecommons.org/licenses/by/4.0/). The use,
distribution or reproduction in other
forums is permitted, provided the
original author(s) and the copyright
owner(s) are credited and that the
original publication in this journal is
cited, in accordance with accepted
academic practice. No use, distribution
or reproduction is permitted which
does not comply with these terms.

High-resolution accessibility and energy cost assessment of 31 priority permanently shadowed regions at the lunar south pole

Yihao Chen¹, Mao Ye^{1,2}, Denggao Qiu¹ and Fei Li^{1,2*}

¹State Key Laboratory of Information Engineering in Surveying, Mapping and Remote Sensing, Wuhan University, Wuhan, China, ²National Gravitation Laboratory, Huazhong University of Science and Technology, Wuhan, China

The permanently shadowed regions (PSRs) at the lunar south pole are primary targets for future robotic exploration and *in situ* resource utilization (ISRU). However, previous accessibility assessments utilizing coarse-resolution orbital data often mask decameter-scale hazards that are critical for surface mobility. In this study, we present a high-resolution accessibility analysis for 31 high-priority PSRs, integrating 5–20 m/pixel Digital Elevation Models (DEMs) with a terramechanics-based rover energy cost model. Using a slope-penalized path planning algorithm, we generated an ensemble of 600 optimal traverses per target to quantify geometric path lengths, slope constraints, and mechanical energy requirements. Our results reveal substantial heterogeneity in accessibility, with median path lengths ranging from ~12 km to ~50 km and minimum round-trip mechanical energy costs spanning an order of magnitude (from ~0.4 kWh to ~4.4 kWh). We demonstrate that geometric proximity does not equate to accessibility; in rugged terrain, safe corridors often require significant detours, rendering theoretical “shortest paths” impassable. Based on accessibility risks, we propose a three-tier prioritization framework: Tier I (e.g., UN11, UN10) offers robust, low-risk access suitable for initial reconnaissance; Tier II requires complex maneuvering through topographic choke points; and Tier III (e.g., Shackleton, Cabeus 2) imposes prohibitive mobility constraints necessitating advanced locomotion capabilities. This study highlights that relying on sub-10 m topography is mandatory for validating operational viability and suggests that “recharge-and-proceed” strategies are essential for deep PSR exploration.

KEYWORDS

high-resolution topography, lunar south pole, path planning, permanently shadowed regions, terramechanics

1 Introduction

Recently, major spacefaring entities—including the US, Europe, Russia, India, Japan, and China—have initiated a new era of lunar exploration focused on the south polar region (e.g., Artemis, Chang’e, Luna, Chandrayaan). A primary scientific objective of these missions is to characterize the abundance and distribution of water ice and other volatiles at the poles. Lunar polar ice not only holds vital clues regarding the origin and evolution of lunar volatiles but also serves as a foundational feedstock for future *in situ* resource utilization (ISRU) and surface life-support systems (Brown et al., 2022; Wang et al., 2024). Consequently, many proposed mission architectures call for robotic explorers to access permanently

shadowed regions (PSRs) near the south pole to map volatile distribution and assess their economic and engineering potential (Cannon and Britt, 2020).

Given that the Moon's spin axis is inclined by only $\sim 1.54^\circ$ relative to the ecliptic normal, solar elevation angles at the poles remain extremely low, keeping the Sun close to the local horizon. This geometric constraint, combined with the rugged topography of the South Pole, creates permanent shadows within crater floors and depressions (Lucey, 2009). These areas function as cold traps, maintaining extremely low temperatures over geological timescales that favor the preservation of water ice and volatiles (Paige et al., 2010a; 2010b). While early theoretical models hypothesized the presence of ice in these PSRs (Watson et al., 1961), subsequent remote sensing has provided a suite of supporting evidence. Notable findings include enhanced same-sense circularly polarized radar backscatter detected by Clementine (Nozette et al., 1996; Spudis et al., 1998) and neutron suppression indicative of hydrogen enrichment observed by Lunar Prospector (Feldman et al., 1998). Furthermore, combined analyses of Diviner thermal data, LOLA altimetry, and M^3 spectral data have constrained near-surface ice distribution to regions where maximum temperatures remain below ~ 110 K (Pieters et al., 2009; Paige et al., 2010a; Mitrofanov et al., 2010; Nozette et al., 2010; Williams et al., 2019; Li et al., 2018). Collectively, these datasets highlight the complex thermophysical properties of the polar regolith and strongly support the presence of volatiles within south polar PSRs (Colaprete et al., 2010; Siegler et al., 2016; Li et al., 2018).

In situ exploration of these regions presents significant engineering challenges. First, regarding accessibility, PSRs are typically nestled within deep impact craters bounded by steep walls. Reaching these targets requires wheeled rovers to descend from high-elevation rims through hazardous terrain, posing severe mobility and traversability risks (Gläser et al., 2014; Brown et al., 2022). Second, in terms of power, the permanent absence of direct solar illumination precludes the use of standard solar arrays. Consequently, operations must rely on radioisotope thermoelectric generators (RTGs) or finite battery storage, which imposes strict constraints on mission duration and traversable range (Sowers and Dreyer, 2019). Finally, communications are constrained by topographic occlusion, which blocks direct line-of-sight (LOS) with Earth. Without the support of orbital relay assets, real-time commanding and high-bandwidth data downlink are severely restricted.

Consequently, quantitatively assessing the accessibility of south polar PSRs has become a critical component of mission planning. Here, accessibility is defined as the feasibility of reaching a target PSR from candidate landing zones, subject to constraints on terrain, illumination, and vehicle performance. While earlier studies qualitatively evaluated representative craters (Gläser et al., 2018; Brown et al., 2022), Cannon and Britt (2020) provided the first systematic analysis of 31 large cold traps. By coupling a rover–regolith interaction model with 40 m/pixel topographic data, they estimated path lengths and energy costs for traversing into these regions. In this work, we target the same set of thermally stable cold traps. Although “PSR” strictly denotes geometric shadowing and “cold trap” implies thermal stability, these features are spatially coincident at the scales relevant to this study. Thus, we adopt the term “PSR” throughout this paper for consistency. A significant

limitation of previous global analyses, however, is the reliance on 40 m resolution data. This resolution is too coarse to resolve meter-to decameter-scale features, inherently smoothing over surface roughness. Crucially, this may mask impassable obstacles—such as localized traps or boulders—leading to an underestimation of traversability risk. To address this gap, we leverage region-specific high-resolution DEMs, including the improved 5 m/pix products from Barker et al. (2021) and standard Lunar Orbiter Laser Altimeter (LOLA) Gridded Data Records (GDRs) (Smith et al., 2010), to reassess the accessibility of these major PSRs. This approach allows for a systematic, internally consistent comparison of targets constrained by realistic, small-scale slope morphology.

To bridge this gap regarding spatial resolution and terrain characterization, this study systematically investigates the accessibility of large lunar south polar PSRs. We identified 31 major exploration targets between 80°S and 90°S by extracting thermally stable cold traps from LRO Diviner summer maximum temperature maps (Williams et al., 2019). These targets were defined as contiguous areas $> 50\text{km}^2$ with summer maximum temperatures $T_{max} \leq 110\text{K}$. To quantitatively assess the accessibility of these identified targets, we leveraged region-specific LOLA products. We utilized the improved 5 m/pix DEMs (Barker et al., 2021) for the high-latitude band ($87\text{--}90^\circ\text{S}$), and standard LOLA Gridded Data Records (GDRs) (Smith et al., 2010) for the $85\text{--}87^\circ\text{S}$ (10 m) and $80\text{--}85^\circ\text{S}$ (20 m) bands. This multi-resolution approach allows us to explicitly resolve critical decameter-scale hazards, including narrow crater rims and localized steep slopes.

Based on these data, we developed a comprehensive path planning framework. We first identified candidate landing zones constrained by local flatness ($\text{slope} < 5^\circ$), illumination duration, and proximity to PSR boundaries. From these zones, multiple traverse routes were generated to reach the PSR interiors. By integrating a rover–regolith interaction model, we quantified the cost of each route in terms of cumulative slope, traverse distance, and energy consumption, resulting in a high-resolution accessibility dataset. Crucially, by re-evaluating the targets from Cannon and Britt (2020) with enhanced resolution and terrain-sensitive energy modeling, we derive representative optimal routes and identify robust, low-risk corridors. The resulting decision framework offers direct quantitative support for landing site selection and ISRU planning in future robotic and crewed lunar campaigns.

2 Materials and methods

2.1 Study area and data sources

The study focuses on the lunar south polar region ($80^\circ\text{S}\text{--}90^\circ\text{S}$), where low solar elevation and rugged topography give rise to extensive permanently shadowed regions (PSRs). Exploration targets were identified using LRO Diviner summer maximum temperature maps derived by Williams et al. (2019). We extracted contiguous zones satisfying $T_{max} \leq 110\text{K}$, a threshold indicating thermal stability for water ice on geological timescales (ice loss rate $< 10\text{cm/Gyr}$; Williams et al., 2019). Filtering for contiguous areas $> 50\text{km}^2$ yielded 31 major PSRs, which serve as the targets for this analysis (Figure 1).

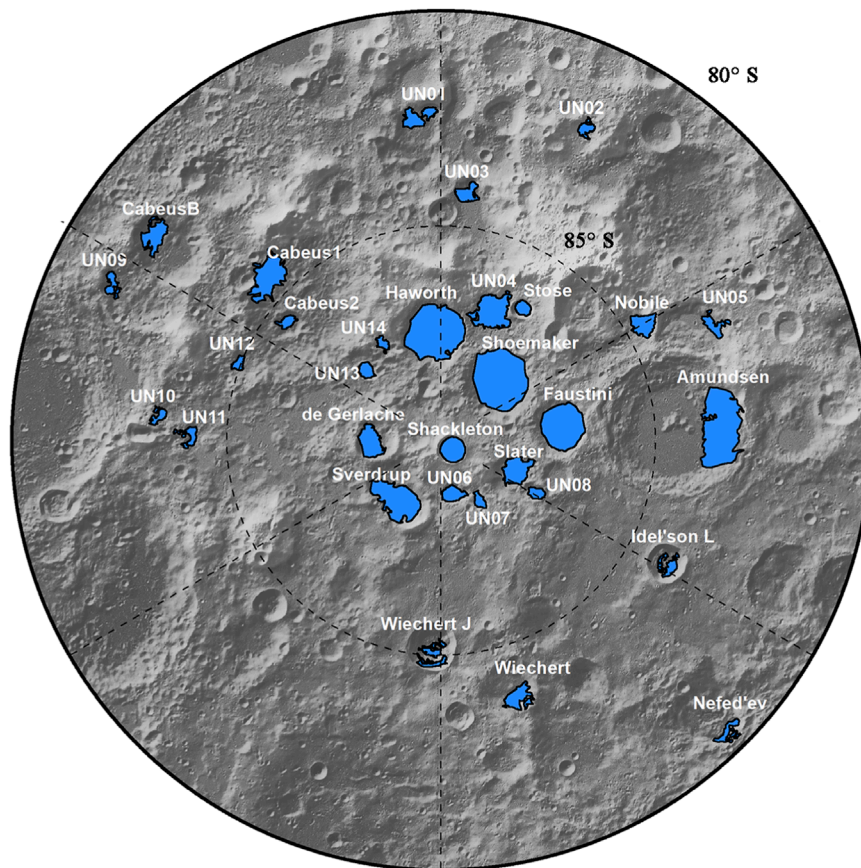


FIGURE 1
Locations of the 31 major PSRs in the lunar south polar region (80°S–90°S). PSRs are shown in blue.

To capture small-scale topographic hazards, we leveraged the highest-resolution LRO/LOLA Lunar Digital Elevation Models (LDEMs) available for each specific region (Barker et al., 2021; Smith et al., 2010). We constructed a composite topographic dataset using the finest nominal resolution for each latitude band. Specifically, for the highest latitudes (87–90°S), we utilized the improved 5 m/pixel DEMs developed by Barker et al. (2021), which utilize iterative orbital track adjustment to correct geolocation errors. For the lower-latitude regions, we employed the standard LOLA GDR products sourced from the Planetary Data System at 10 m/pixel (85–87°S) and 20 m/pixel (80–85°S) resolutions (Smith et al., 2010). All products share a consistent south polar stereographic projection and geodetic datum. Unlike previous studies that relied on uniform 40 m grids (e.g., Cannon and Britt, 2020), this multi-resolution approach enables the detection of critical mobility barriers, including decameter-scale slope breaks, terraces, and narrow choke points along crater rims.

For lighting constraints, we utilized the average illumination maps from Mazarico et al. (2011). These products quantify the fraction of time a surface is illuminated over an 18.6-year precessional cycle (simulated at 1-h intervals). We employed the 75–90°S raster at ~120 m/pixel resolution to provide a broad-scale context for screening and selecting persistent illumination patches suitable for landing, prior to detailed traverse planning.

2.2 DEM preprocessing and slope calculation

LOLA-derived DEMs were processed in their native south polar stereographic projection at original spatial resolutions (5–20 m) to preserve topographic fidelity (Smith et al., 2010). No resampling was applied. Invalid data points (no-data pixels) were masked during computation to prevent boundary artifacts and restored in the final outputs to maintain spatial consistency.

Slope maps were generated using a second-order finite difference method. We employed the 3×3 weighted central-difference algorithm (Horn, 1981) for internal grid points, which provides a robust estimate of surface gradients by reducing sensitivity to high-frequency noise. At image boundaries, the scheme adapts to one-sided differences. The horizontal partial derivatives, $\partial z/\partial x$ and $\partial z/\partial y$, were computed using the native grid spacing as the step length.

The local slope angle θ was then derived as:

$$\theta = \arctan \sqrt{\left(\frac{\partial z}{\partial x}\right)^2 + \left(\frac{\partial z}{\partial y}\right)^2}$$

Slopes are reported in degrees to align with standard engineering criteria for landing safety and rover traversability (Rosenburg et al., 2011). This preprocessing pipeline ensures

that the resulting slope fields are free of boundary artifacts and suitable for the subsequent landing zone selection (Section 2.3) and traversability analysis (Section 2.4).

2.3 Identification of candidate landing regions

Candidate landing regions were delineated for each target PSR by spatially intersecting specific constraints on terrain safety, illumination, and proximity. To ensure safe landing and initial rover deployment, we first enforced a strict terrain constraint, excluding all pixels with slopes exceeding 5° . We deliberately selected this conservative slope threshold, which is stricter than the 8° engineering limit of the Chang' E-3 mission (Sun et al., 2014), to rigorously account for DEM smoothing effects and data uncertainty. Simultaneously, to facilitate solar-powered operations and survival, landing sites were required to satisfy a long-term average illumination fraction of $>40\%$ over the 18.6-year precessional cycle (Mazarico et al., 2011). This threshold represents a practical trade-off between target availability and operational suitability. From an engineering perspective, high average illumination correlates with reduced maximum eclipse durations (Speyerer and Robinson, 2013), thereby facilitating frequent recharging and mitigating the risks associated with extended darkness. Our spatial analysis demonstrated that while applying higher thresholds (e.g., testing a 50% requirement) yielded negligible suitable areas for some targets, this 40% baseline provides a robust starting condition for the rover while maintaining broad target accessibility.

Finally, proximity constraints were applied to ensure the PSRs are reachable within a reasonable traverse distance while avoiding steep crater walls. For crater-hosted PSRs, the search area was limited to a 10 km buffer extending outward from the rim crest of the host crater, defined to constrain the traverse distance within operational limits. In contrast, for irregular PSRs not confined to a single major crater, we employed an annular search zone extending 10–20 km from the PSR boundary. The final candidate landing regions correspond to the spatial intersection of these three masks, serving as the initialization points for the path-planning framework described in Section 2.4.

The environmental constraints and the resulting selection of landing zones are illustrated in Figure 2. Specifically, the topographic slope (Figure 2a) and average illumination conditions (Figure 2b) within the 80°S – 90°S region were analyzed to identify suitable landing areas, which are highlighted in red in Figure 2c.

2.4 Path-planning framework

Traverse analysis was conducted using a grid-based least-cost path method (Dijkstra, 1959; Speyerer et al., 2016). For each PSR, we established a randomized sampling strategy to characterize accessibility: 100 start points were sampled from candidate landing regions (minimum separation: 100 m), and 6 goal points were sampled from flat terrain ($\theta_{deg} \leq 5^\circ$) within the PSR interior. This yielded 600 start–goal combinations per target.

The path planning operates on an 8-connected grid graph, where nodes represent valid DEM pixels and edges connect orthogonal and diagonal neighbors. Pixels with slopes exceeding 35° were

masked as non-traversable. This threshold is not an operational safety margin but a physical upper bound motivated by the internal friction angle of typical lunar regolith (Carrier et al., 1991), beyond which shear failure is expected and sustained traction becomes infeasible. In contrast, nominal landing and roving operations typically adopt much gentler limits to mitigate rollover risk (e.g., 15° ; Sathyan et al., 2024). However, accessing the extreme terrain of PSRs requires a path-planning framework capable of evaluating the absolute physical limits of wheeled locomotion before applying operational safety buffers. To ensure robustness against local data artifacts, start and goal coordinates falling on invalid pixels were snapped to the nearest valid pixel within a 3-pixel radius.

Optimal paths were calculated using Dijkstra's algorithm (Dijkstra, 1959; Zhou et al., 2014; Speyerer et al., 2016). To maximize computational efficiency given the “many-starts, few-goals” configuration, we implemented a reverse-expansion strategy (goal-as-source). For each goal, a single Dijkstra propagation computes the minimum-cost tree to all potential start nodes, reducing the required distinct searches from 600 to 6 per target.

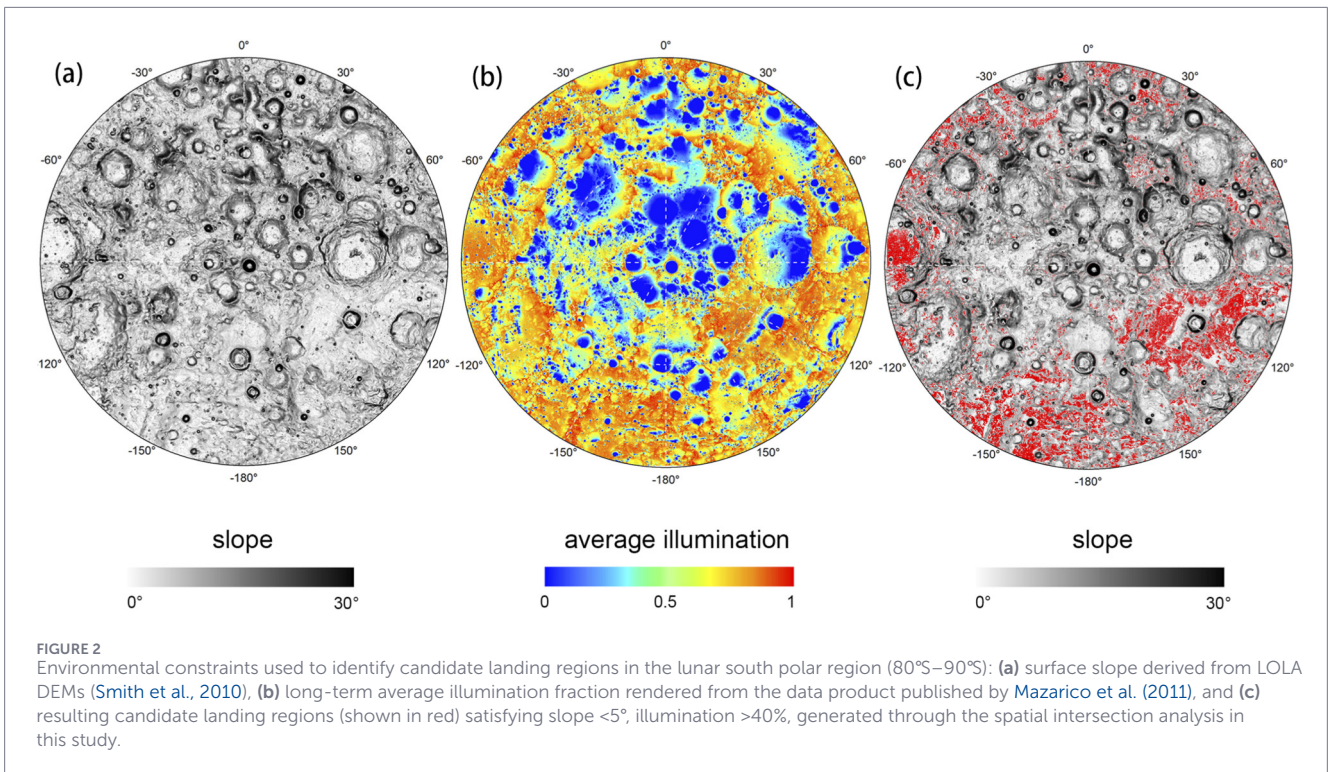
To address the specific topographic challenges, we introduced a custom penalty function in this study. The traversal cost C between a current pixel u and a neighbor v is defined to penalize steep slopes:

$$C(u, v) = d \cdot (1 + k_{slope} \cdot \theta_{uv})$$

Here, d denotes the geometric distance between adjacent pixels. Specifically, d equals the spatial resolution R for orthogonal transitions and $\sqrt{2}R$ for diagonal transitions. The variable θ_{uv} represents the directional slope evaluated between the centers of the adjacent pixels in degrees. To address the fact that physical traversal risk increases non-linearly with slope, we implemented a decoupled feasibility and optimality strategy in our cost formulation. For feasibility, we enforced an absolute physical mobility limit by masking all pixels exceeding 35° . As established by the internal friction angle of loose lunar regolith (Carrier et al., 1991), this threshold acts as an impassable barrier with infinite cost. For optimality within the remaining traversable domain (0 – 35°), we utilized a linear cost function where the slope penalty coefficient k_{slope} was set to 2.0. A linear penalty may underrepresent risk near stability limits, but it produces a well-conditioned, monotonic cost surface that is numerically stable for graph search. Exponential penalties can create an excessive dynamic range (overflow or near-infinite costs) and thus act as artificial barriers, potentially preventing path discovery despite physically feasible corridors.

2.5 Rover–regolith interaction and energy cost model

To quantify the mechanical energy required for a rover to traverse a given path, we adopt a classical terramechanics framework for lunar vehicles, in which the interaction between the rover wheels and the regolith is decomposed into three main components: soil compaction resistance R_c , bulldozing resistance R_b , and gravitational resistance R_g (Bekker, 1956; Bekker, 1969). These components together determine the total traction effort (TTE) needed to maintain quasi-steady motion along a slope (Carrier et al., 1991; Carrier, 2003; Wong and Reece, 1967; Wong and Reece, 2001). For a representative wheel of width b , radius



r , and normal load W_w , R_c and R_b are functions of the soil cohesion c , internal friction angle ϕ , bulk unit weight γ , and deformation moduli k_c and k_ϕ , while R_g depends on the total vehicle weight W_v and the local slope angle θ . Several intermediate quantities in these expressions—such as the wheel sinkage z , approach angle α , failure-wedge length l_0 , the deformation modulus k_c , and the bearing-capacity factors N_γ , N_c , and N_q —are standard functions of c , ϕ , γ , W_w , and r derived from the geometry and force balance of the wheel–soil system (Carrier et al., 1991; Carrier et al., 2003). The explicit functional forms adopted in this study are detailed in Supplementary Section S1 (Equations 1–13). This classical framework matches the empirical behavior observed during the Apollo missions. On flat, loose regolith, the energy cost is dominated by soil compaction (R_c) and bulldozing (R_b) resistances due to wheel sinkage. Conversely, on steep slopes, the gravitational component (R_g) becomes the governing factor. By explicitly modeling these components, our framework prevents the path planner from underestimating costs on flat but soft terrain, a capability that simpler slope-only cost functions lack.

The explicit functional forms for these intermediate quantities are provided in Supplementary Section S1. This classical framework matches the empirical behavior observed during the Apollo missions. It effectively captures the physical reality where energy cost is dominated by soil compaction (R_c) on flat terrain, but transitions to being dominated by gravitational resistance (R_g) on steep slopes, reflecting the governing mechanics of lunar surface mobility.

In our implementation, we treat R_c and R_b as per-wheel resistances at the representative wheel–soil contact and R_g as acting at the vehicle level. For a rover with n wheels, the total traction effort TTE is obtained by combining these three components following the standard terramechanics formulations cited above. The soil

TABLE 1 Summary of lunar regolith properties and rover specifications used in the energy model.

Parameters	Value
Coefficient of soil cohesion, c	170N/m ²
Soil friction angle, ϕ	35°
Exponent of soil deformation, n_0	1 (dimensionless)
Cohesive modulus of soil deformation, k_c	1400N/m ²
Frictional modulus of soil deformation, k_ϕ	820000N/m ³
Soil density, γ	2470N/m ³
Lunar rover mass, m	500 kg
Lunar rover weight, W_v	810N
Lunar rover weight on wheel, W_w	202.5N
Lunar rover wheel width, b	25 cm
Lunar rover wheel radius, r	40 cm
Lunar rover wheel's number, n	4

parameters (e.g., cohesion, internal friction angle, deformation moduli, bulk density) are adopted from analyses of Apollo and Soviet lunar mission data (Mitchell et al., 1974), whereas the rover structural parameters (mass, wheel dimensions, wheel load, and number of wheels) are chosen to be representative of a mid-sized polar rover; all parameter values are summarized in Table 1.

For each step along a raster path, from pixel v to pixel u , we compute the directional slope θ along the traverse vector derived from the DEM. Recognizing that the DEM resolution varies (5 m, 10 m, or 20 m) depending on the latitude and that

slope is a scale-dependent parameter, we strictly separate our subsequent analysis and ranking by resolution band to ensure rigorous comparability (see Section 3). We then use this θ to evaluate the corresponding *TTE* and approximate the incremental mechanical energy required to traverse that step as the product of *TTE* and the geometric step length d between \mathbf{v} and \mathbf{u} . By summing these incremental contributions along a given path, we obtain the total mechanical energy required for the rover to follow that traverse under the assumed soil and vehicle conditions. In this study, soil and vehicle parameters are assumed to be spatially uniform within each study area, so that the dominant spatial variability in energy cost arises from changes in slope θ and path geometry d . The resulting energy estimates are used primarily for relative comparison among PSRs and trajectories (within the same resolution band), rather than as exact end-to-end mission power budgets, because effects such as variable speed, wheel slip, thermal control, and communication loads are not explicitly modeled. Furthermore, we acknowledge that the DEM resolution (up to 20 m) is coarser than the rover's wheelbase (~2 m), meaning that sub-pixel hazards (e.g., small boulders) are not geometrically resolved. Therefore, our calculated costs represent a baseline estimate dominated by macro-topography and soil mechanics. In a flight mission, these sub-pixel features would be managed by on-board hazard avoidance systems, potentially introducing minor local variations to the total path length.

2.6 Accessibility metrics and statistical analysis

For each of the 31 target PSRs, the path-planning and energy models described above yield an ensemble of 600 traverses (100 start points \times 6 goal points), each characterized by specific geometric and energetic metrics. Building on this dataset, we define a set of quantitative accessibility indicators to perform a systematic statistical comparison across the targets.

For every start–goal pair, the geometric path length L is computed as the sum of step lengths along the minimum-cost trajectory returned by the slope-penalized Dijkstra search (Section 2.4). Path lengths are expressed in kilometers. For each PSR, the distribution of L across the 600 simulations is summarized by the minimum, 25th percentile (P25), median, 75th percentile (P75), maximum, and interquartile range (IQR = P75 – P25). The median path length serves as the primary length-based ranking indicator, while the IQR characterizes the variability of path length arising from different start–goal configurations. These length distributions are visualized using violin plots and boxplots with a common vertical scale to facilitate direct comparison among PSRs.

To capture both local and global topographic constraints, we derive two slope statistics for each traverse: the maximum slope θ_{max} encountered along the path and the mean slope θ_{mean} , obtained by averaging the local slope angles over all steps (where the step length corresponds to the Euclidean distance between consecutive pixel centers, being R the spatial resolution for orthogonal and $\sqrt{2}R$ the one for diagonal transitions respectively). For each PSR, we first quantify the fraction of paths where θ_{max} exceeds a safety threshold (set to 25° in this study). This threshold is used as a post-processing classification metric rather than a physical mobility limit.

It was chosen to provide a conservative 10° engineering buffer below the 35° physical failure bound, thereby maintaining operational margin against potential wheel slip and local data uncertainty. Sensitivity analyses (Supplementary Material Section S6) further show that, although varying this threshold shifts the boundary between moderate- and high-risk categories, the set of top-priority Tier I candidates remains fully invariant, indicating that our primary exploration recommendations are robust to this parameter choice. This fraction serves as a proxy for the availability of low-risk corridors, indicating the proportion of routes forced to navigate hazardous terrain. Second, we define the minimum of the maximum slope $\min(\theta_{max})$ as the lowest peak slope observed across the ensemble of 600 paths. This metric effectively determines whether at least one gentle, low-risk corridor exists for a given PSR. The distributions of θ_{max} and θ_{mean} are summarized by their medians and IQRs and displayed as boxplots (Figures 6, 7), allowing us to differentiate between targets dominated by globally steep terrain profiles and those characterized by generally moderate slopes punctuated by short, steep segments.

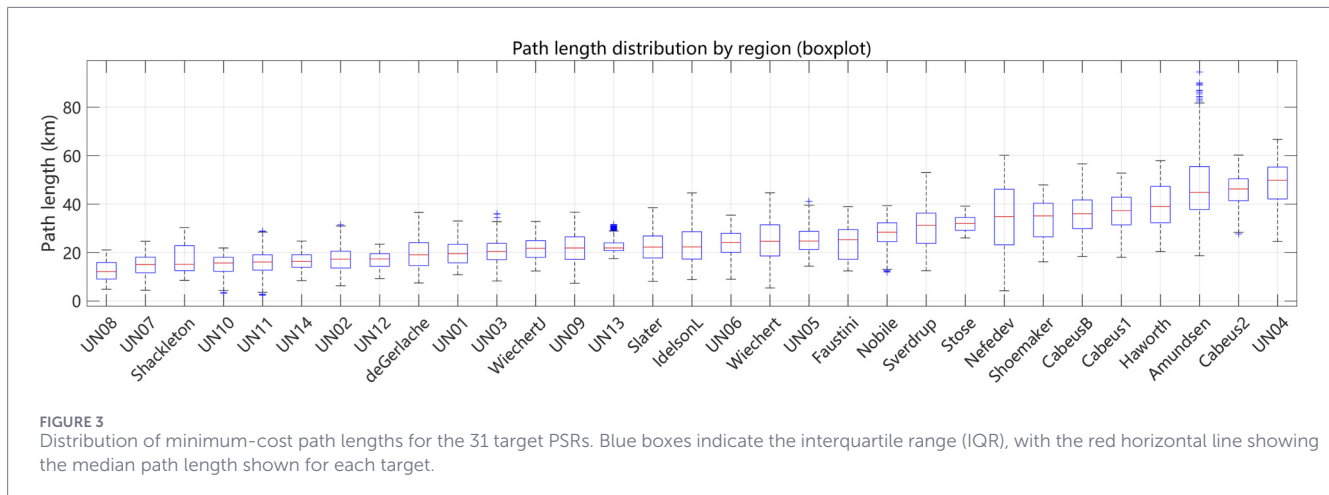
In addition to geometric indicators, we derive energy-based metrics using the rover–regolith interaction model (Section 2.5). For each step from pixel \mathbf{u} to \mathbf{v} , the incremental energy is summed along the path to obtain the total traversal energy. Since the gravitational resistance component is direction-dependent, uphill and downhill segments exhibit energetic asymmetry. To capture this at the mission level, we distinctively analyze departure legs (from landing regions into the PSR) and return legs (from the PSR back to the landing regions). For each PSR, we search the path ensemble to identify the minimum departure energy $E_{dep,min}$, the minimum return energy $E_{ret,min}$, and the corresponding minimum round-trip energy $E_{rt,min}$. The latter represents the most energetically favorable closed-loop traverse (assuming the rover retraces its path) between the landing zone and the target PSR. These three quantities constitute our core energy-based indicators. These three quantities constitute our core energy-based indicators, and the specific calculated values for all 31 target PSRs are comprehensively reported in Supplementary Material Table S3 within Section S7.

Consequently, each PSR is characterized by a triplet of primary accessibility indicators: median path length, minimum peak slope $\min(\theta_{max})$, and minimum round-trip energy $E_{rt,min}$, supported by auxiliary distributional metrics. PSRs are ranked in ascending order for each primary indicator, where shorter paths, lower peak slopes, and lower energy costs are considered more favorable. We then perform a comparative assessment to examine the trade-offs among these three dimensions and identify PSRs that consistently score well across length, slope, and energy criteria. This joint interpretation is utilized in subsequent sections to highlight candidate low-risk corridors and to propose a qualitative prioritization scheme for future south polar exploration targets.

3 Results

3.1 Path length

For each of the 31 target PSRs, we analyzed the distribution of geometric path lengths derived from the ensemble of 600 minimum-cost traverses (representing all start–goal combinations calculated



in Section 2). To verify that these trajectories are not artifacts of elevation uncertainties, we performed Monte Carlo sensitivity analyses on synthetic terrain clones injected with Gaussian noise scaled to the error models of Barker et al. (2021), Barker et al. (2023). As detailed in Supplementary Material Section S3, the 100% traversal success rate in these stress tests proves that the identified corridors remain structurally stable even under worst-case roughness. As illustrated in Figure 3, the median path lengths across the targets range from approximately 12–50 km, exhibiting substantial variability. The figure also reports the interquartile range (IQR) for each distribution, characterizing the spread of the central 50% of the data. For most PSRs, the IQR remains moderate, indicating that the minimum-cost path length is relatively constrained regardless of the specific start–goal pairing.

When ranked by median path length (Figure 3; Supplementary Material Table S2), the most accessible targets are UN08 (12.20 km), UN07 (15.09 km), Shackleton (15.17 km), UN10 (15.71 km), and UN11 (16.14 km), with IQRs ranging from 5.8 to 10.4 km. Conversely, the targets requiring the longest traverses are Cabeus1 (37.33 km), Haworth (39.09 km), Amundsen (44.93 km), Cabeus2 (46.32 km), and UN04 (49.86 km). These contrasts reflect the combined influence of proximity and topography: PSRs located near accessible crater terraces with gentler intervening terrain minimize the need for detouring, thereby yielding favorable length statistics.

Using the IQR to assess internal variability (Supplementary Material Table S2), UN13, UN14, and UN12 exhibit the most consistent path lengths, with IQRs of 3.27 km, 5.15 km, and 5.23 km, respectively. This suggests that their accessibility is robust to the choice of landing site. In contrast, PSRs with larger IQRs, such as Amundsen (IQR = 17.73 km) and Nefedev (IQR = 22.92 km), likely possess complex crater-wall geometries or step-like topography. In such terrains, the path planner must trade off between “short but steep” and “long but gentle” trajectories depending on the specific endpoint, creating distinct routing corridors that broaden the upper tail of the length distribution.

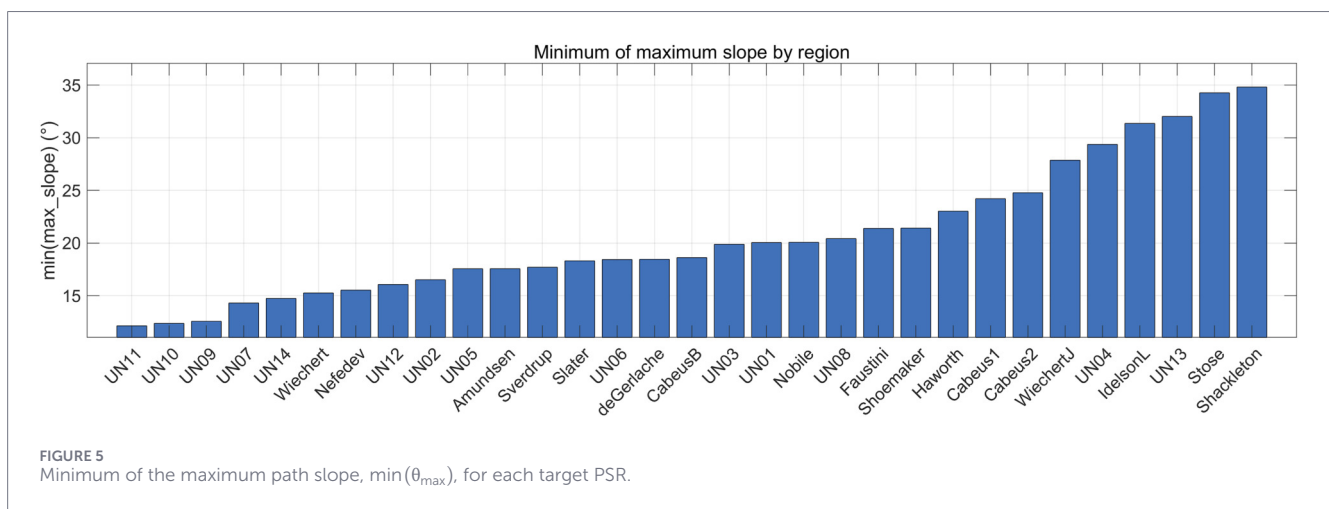
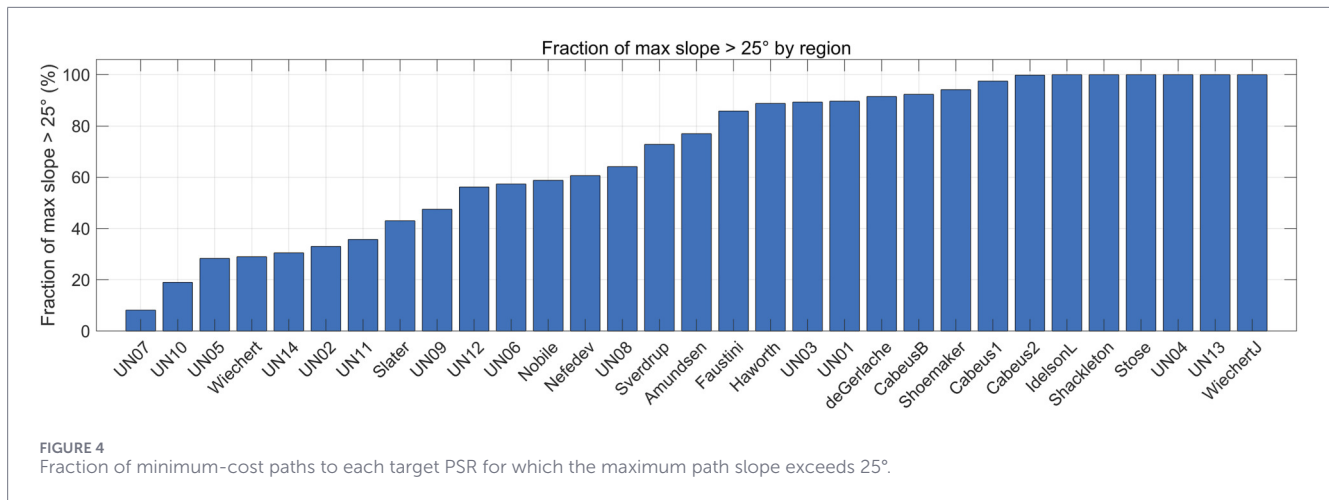
3.2 Path slope

Given that safe rover operations necessitate avoiding high-risk terrain, we next assess the accessibility of the 31 target PSRs

based on path slope constraints. We employ three complementary metrics: (1) the fraction of paths for which the maximum slope θ_{max} exceeds 25° (as justified in Section 2.6), used as a proxy for the necessity of traversing hazardous terrain; (2) the lowest peak slope observed across all paths, denoted as $\min(\theta_{max})$, which indicates the existence of at least one gentle “seed corridor”; and (3) the statistical distributions of both maximum and mean slopes, which disentangle “peak risk” from overall terrain steepness.

As shown in Figure 4, we first examine the fraction of minimum-cost paths whose peak slope θ_{max} exceeds the 25° hazard threshold. Because each path is already optimized to penalize slope, a high exceedance fraction indicates that low-slope corridors are geometrically scarce: even the best available routes frequently include segments steeper than 25° . Conversely, a low exceedance fraction implies substantial geometric redundancy, i.e., multiple alternative corridors that remain below the hazard threshold for different start–goal configurations. This redundancy is particularly valuable in the lunar polar environment, where illumination conditions vary with time and can temporarily invalidate a planned traverse. Although illumination is not explicitly modeled here, targets with more geometrically safe alternatives are expected to offer greater operational flexibility: if a preferred corridor becomes unavailable due to transient shadows, other comparably safe corridors are more likely to exist. Consistent with this interpretation, targets such as UN07, UN10, UN05, Wiechert, and Slater show exceedance fractions below 50%, whereas Wiechert J, UN13, UN04, Shackleton, and Cabeus1/2 exceed 90%, implying that avoiding steep terrain is difficult regardless of corridor choice and that mission planning may require larger detours, reduced speeds, or enhanced mobility capabilities.

To identify potential low-risk access routes, Figure 5 further presents the $\min(\theta_{max})$ for each PSR. This metric verifies whether a PSR possesses at least one “seed corridor” suitable for initial exploration. We find that UN11, UN10, UN09, UN07, and UN14 all exhibit $\min(\theta_{max})$ values below 15° , confirming the presence of highly favorable access routes. Because these targets are predominantly located at relatively lower polar latitudes where the effective LDEM resolution can be coarser and terrain may appear smoother, we explicitly evaluated the sensitivity of this result to potential resolution-induced slope underestimation.



Specifically, we repeated the analysis for all targets using a uniform 20-m DEM and found that the three-tier classification remained almost unchanged (Supplementary Material S2); additionally, a Monte Carlo “roughening” test on UN10 (a worst-case example) showed negligible impacts on connectivity and only minor biases in path metrics (Supplementary Material S3). Conversely, PSRs such as Wiechert J, UN04, Idelson L, and Shackleton yield $\min(\theta_{max})$ values exceeding 25°, implying that even the most optimal trajectories are constrained by unavoidable steep segments.

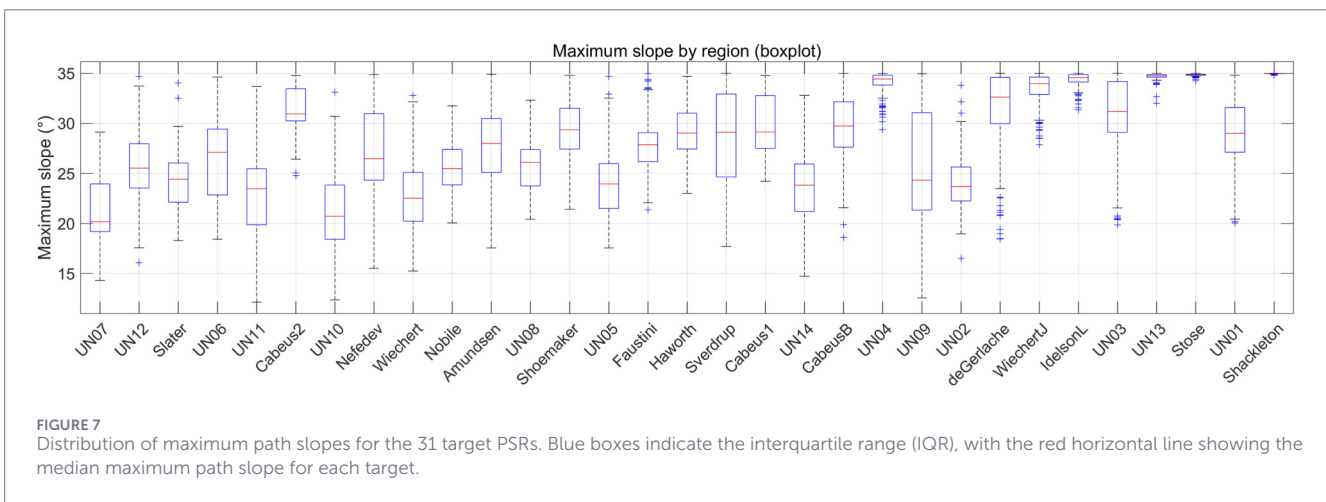
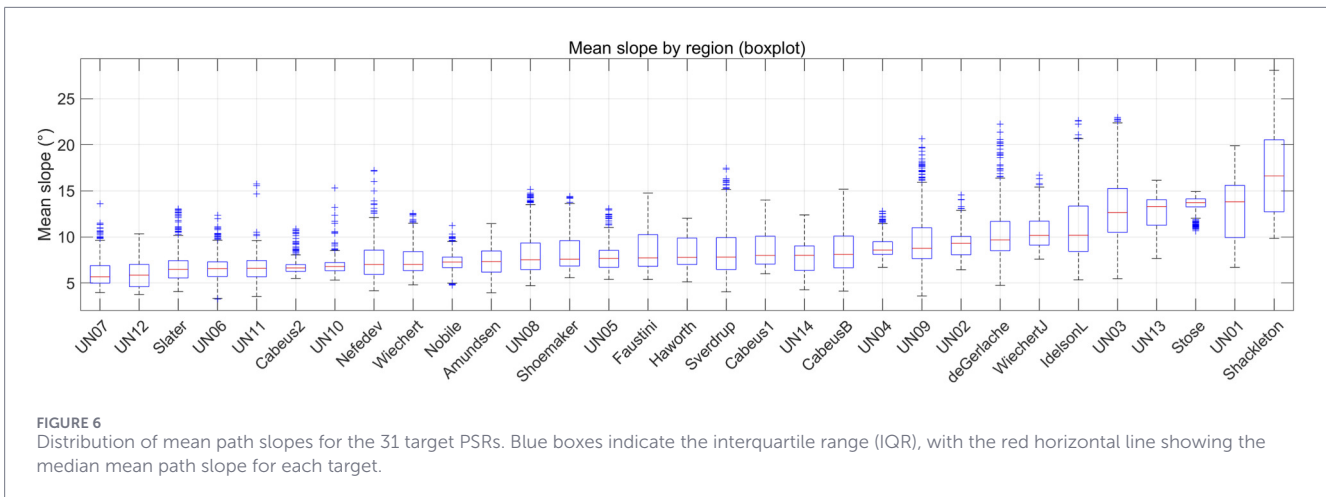
Finally, we compare the distributions of peak risk θ_{max} and average steepness θ_{mean} to characterize the terrain roughness (Figures 6, 7). While the median mean slopes θ_{mean} are relatively moderate and consistent across most PSRs, the corresponding θ_{max} distributions reveal significant disparities, with some targets showing modest mean slopes but pronounced upper tails in θ_{max} . This pattern suggests that routes are globally manageable but include localized steep segments at the DEM sampling scale. Because the effective resolution of polar LDEMs can be coarser than the nominal pixel spacing, using a coarser baseline (i.e., effective-resolution slopes) would act as a low-pass filter and may smooth out small-scale but mission-critical hazards

(e.g., short crater-wall segments). We therefore retain pixel-wise slope estimates as a conservative representation for hazard characterization, where overestimating local steepness leads to safer detours rather than underestimating potential obstacles. Importantly, our sensitivity analyses (Section 4.4) indicate that this pixel-level treatment does not invalidate the accessibility assessment: even under worst-case perturbations, robust corridors can still be identified and the overall interpretation remains stable.

Collectively, these joint distributions reveal distinct accessibility classes: some PSRs offer broad, low-risk corridors, while others are guarded by steep crater walls necessitating complex maneuvers. These quantitative differences provide the physical basis for the prioritization framework discussed in Section 4.

3.3 Path energy

From an engineering perspective, we evaluate the mechanical energy required for a round-trip traverse between candidate landing regions and the interior of each PSR. As defined in Section 2.6, we directly analyze three key indicators for each target: the minimum departure energy $E_{dep,min}$, the minimum return energy $E_{ret,min}$, and the minimum round-trip energy $E_{rt,min}$.



Supplementary Table S3 in Supplementary Material S7 summarizes the results, sorted by increasing round-trip energy cost. The estimated $E_{rt,min}$ values span an order of magnitude, ranging from approximately $\times 1.410^6$ J to 1.6×10^7 J. Targets such as UN11, UN10, Nefedev, UN07, and UN08 fall at the lower end of this spectrum, indicating that a complete sortie is energetically feasible with comparatively modest resources. In contrast, PSRs such as Cabeus 2, Stose, Amundsen, Haworth, and UN04 occupy the upper tail of the distribution, exhibiting substantially higher energy costs (Supplementary Table S3 in Supplementary Material S7). For these targets, mission planners must carefully weigh the potential scientific return against the escalated locomotion and power storage requirements.

It is important to note that these values represent idealized mechanical energy based on spatially uniform regolith properties. Since operational factors such as wheel slip, thermal control, and communication loads are not explicitly modeled, the reported energies should be interpreted as relative indices for ranking accessibility rather than as precise end-to-end mission power budgets. Within this comparative framework, however, the data explicitly highlight which PSRs offer the most energetically efficient targets for future surface exploration.

4 Discussion

4.1 Prioritization of exploration targets based on accessibility risks

To translate the quantitative accessibility metrics derived in Section 3 into actionable mission planning strategies, we propose a three-tier classification framework for the 31 target PSRs. This framework integrates the overall traversability of the surrounding terrain (represented by the fraction of paths with slope $>25^\circ$) and the feasibility of safe access corridors (represented by the minimum peak slope, $\min(\theta_{max})$). A comprehensive summary of this classification, detailing the core geometric and energetic characteristics for all targets across Tier I, Tier II, and Tier III, is presented in Supplementary Material Table S5 within Section S7. By synthesizing these indicators, we distinguish between targets that offer robust, high-margin access and those that impose severe constraints on surface mobility systems.

Tier I (Priority A) represents the most favorable category, exemplified by targets such as UN11, UN10, UN09, UN07, and UN14. These regions are characterized by a negligible fraction of steep paths and a $\min(\theta_{max})$ well below 15° . From an engineering perspective, these PSRs are prime candidates for initial robotic

reconnaissance and potential base establishment. The benign terrain allows for high-margin traverse planning, minimizing the need for complex autonomous hazard avoidance. Furthermore, the distinct low-slope corridors identified in these regions could likely serve as reusable supply routes for long-term ISRU operations, offering the highest operational efficiency for infrastructure development.

Tier II (Priority B) occupies the intermediate range, including Wiechert, Nefedev, and UN12. These PSRs exhibit moderate accessibility, typically requiring traverses over segments with slopes between 15° and 25°. While physically accessible to standard wheeled rovers, these regions necessitate rigorous route optimization to navigate specific “choke points” where mobility risks are elevated. Consequently, these targets are best suited for follow-up missions where specific scientific returns—such as unique volatile composition or geological context—justify the increased operational complexity and risk exposure compared to Tier I targets.

Tier III (Priority C), including Shackleton, Stose, UN13, Idelson L, UN04, and Wiechert J, represents the most logistically challenging options. Characterized by extensive high-slope terrain (fraction of steep paths >90%) and a $\min(\theta_{max})$ exceeding 25°, these regions are largely inaccessible to conventional wheeled platforms, which would face prohibitive risks of excessive slippage or mechanical instability. Exploration of these targets would likely necessitate specialized mobility concepts, such as hopping robots, tethered systems, or walking mechanisms. Unless the scientific value is exceptionally compelling, these targets should be deprioritized in near-term mission roadmaps in favor of more accessible alternatives.

4.2 Case studies: trade-offs between path geometry and safety

To visually investigate the trade-offs between path length and terrain risk, we examined the specific traverse geometries within our generated path ensembles. Figure 6 presents the routing results for representative targets from different accessibility tiers, overlaid on high-resolution slope maps. In these visualizations, the yellow trajectories identify the geometrically shortest path among the 600 generated simulations, while the green trajectories represent the “safest” path—specifically, the trajectory that minimizes the maximum slope $\min(\theta_{max})$ across the ensemble. Comprehensive traverse maps for the remaining 29 target regions are provided in the Supplementary Material S7 (Supplementary Figure S7–S35).

Figure 8A illustrates the scenario for UN07 (Tier I). Here, the terrain between the landing zone and the PSR boundary is remarkably benign. Consequently, although the two paths are spatially distinct, the safest path (green) does not require a significant detour compared to the shortest path (yellow). This observation indicates that for Tier I targets, the “cost” of safety is minimal; high-safety trajectories are available without incurring a substantial penalty in path length.

In stark contrast, Figure 8B depicts the rugged environment of UN04 (Tier III). The divergence between the two trajectories is striking. The shortest path (yellow) attempts a direct approach but inevitably intercepts crater rim segments with prohibitive slopes (>25°), rendering it physically impassable. The safest path (green), however, diverges significantly, performing a tortuous detour to exploit a narrow, fragmented low-slope corridor.

This comparison visually underscores a critical finding: in complex polar terrain, geometric proximity does not equate to accessibility. The substantial difference between the yellow and green trajectories in difficult regions demonstrates that prioritizing safety (minimizing peak slope) often incurs a significant penalty in path length. By resolving these decameter-scale hazards, our analysis confirms that realistic traverses to deep PSRs generally require significantly longer distances and higher energy budgets than idealized geometric estimates suggest.

4.3 Energy implications for rover mission architecture

The energy analysis (Section 3.3) places stringent constraints on the design of future polar rovers. Converting our mechanical energy estimates into electrical units, the minimum round-trip requirements for Tier I targets range from approximately 0.4 kWh to 4.4 kWh (Supplementary Material Table S3 within Section S7).

To contextualize these values, a mid-sized solar-powered lunar rover (e.g., VIPER-class) typically carries battery storage on the order of several kWh (e.g., ~5.4 kWh for VIPER at beginning of life, 0 °C), with solar arrays providing a few hundred watts of generation (Bluethmann, 2024). This comparison reveals a critical challenge: for even the most accessible Tier I targets, the required mechanical energy alone rivals the total onboard energy storage. Considering that mobility typically constitutes only a fraction of the total power budget—with significant margins required for thermal management, communication, and payload operations—the energy demand for a single continuous sortie far exceeds current battery capabilities.

This disparity implies that a simple “sprint” strategy—driving directly into the PSR and back on a single charge—is likely unfeasible for most targets without supplemental power sources (e.g., RTGs or tethered power). Instead, solar-powered mission architectures must rigorously prioritize “recharge-and-proceed” strategies during the approach phase, utilizing illumination corridors to maintain state-of-charge before the final traverse into darkness. Furthermore, for ISRU missions, the Energy Return on Investment (EROI) becomes a governing factor. If the energy expended to retrieve volatiles from a deep, high-friction Tier III PSR exceeds the energy equivalent of the extracted resources, the target becomes economically unviable regardless of its ice abundance (Rubanenko et al., 2019).

4.4 Sensitivity to data quality and physical constraints

To explicitly address potential biases arising from mixed DEM resolutions, we first conducted a comprehensive control experiment using the official LOLA GDR 20 m/pixel dataset as a uniform benchmark. We re-executed the complete path-planning pipeline for all 31 targets, generating a control dataset of 18,600 trajectories. The results (summarized in Supplementary Material Figure S1) demonstrate that the macro-scale accessibility ranking is exceptionally robust, yielding a near-perfect Spearman rank correlation ($\rho = 1$) between the mixed-resolution and uniform-control datasets. However, the analysis also confirms that coarser resolutions systematically “smooth out” steep terrain features, underestimating peak slopes by an average of 0.9°. This validates

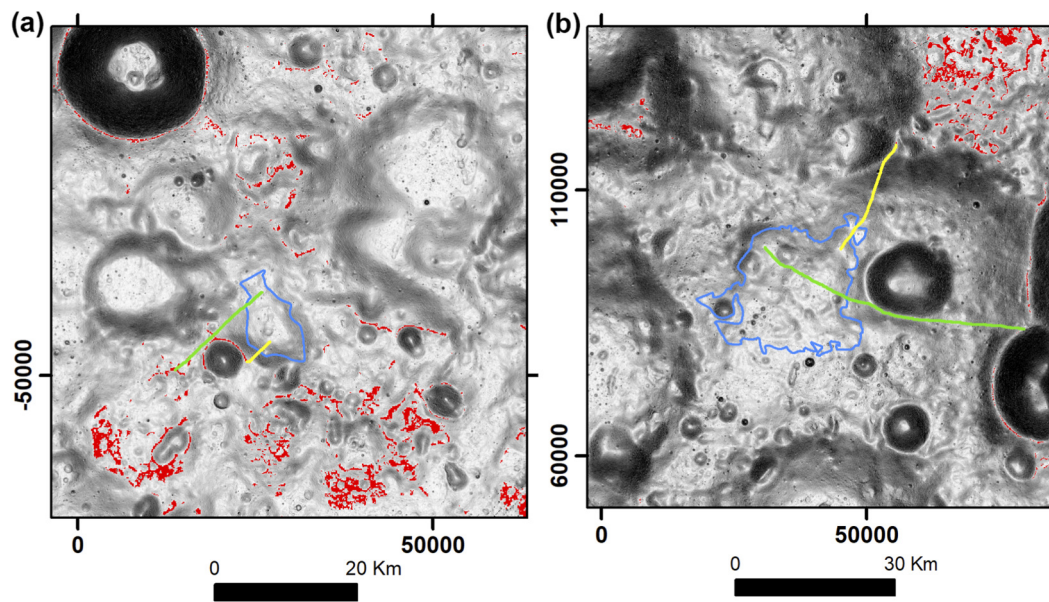


FIGURE 8

Comparison of shortest and safest rover traverses for representative PSRs, shown on high-resolution slope maps. Yellow trajectories represent the shortest paths, and green trajectories represent the safest paths minimizing peak slope $\min(\theta_{max})$. Blue curves delineate the boundaries of the target PSRs, while red areas indicate the designated suitable landing zones. Panels illustrate (a) UN07 (Tier I) and (b) UN04 (Tier III).

our methodological choice: while 20 m data is sufficient for strategic ranking, the high-resolution (5–10 m) models used in this study are mandatory for detecting operational hazards and preventing the risk-masking effect.

Complementary to the resolution analysis, to rigorously validate the robustness of our accessibility rankings against data quality variations—particularly the inherent “smoothing effect” of lower-latitude DEMs—we conducted a comparative Monte Carlo sensitivity analysis across three representative regions: UN07 (High-latitude, 5 m/pix), Nobile (Mid-latitude, 10 m/pix), and UN10 (Low-latitude, 20 m/pix). For each target, we generated an ensemble of 50 synthetic terrain clones by superimposing pixel-wise independent Gaussian noise onto the baseline DEM, scaled by the local vertical RMSE derived from Barker et al. (2023). This approach ($Z_{new} = Z_{old} + \mathcal{N}(0, 1) \cdot \sigma_{ERR}$) maximizes local surface roughness, serving as a conservative “worst-case” stress test for the rover’s mobility constraints.

The simulation results (visualized in Supplementary Figure S2 and summarized in S7 Supplementary Table S3) demonstrate a high degree of robustness across the full latitude spectrum. The path planner achieved a 100% success rate in identifying valid traverses across all 150 simulations. Crucially, for the lowest-resolution target (UN10), which represents the highest uncertainty scenario, the impact on primary mission metrics was minimal. The average path length exhibited a slight negative bias (−0.36%) due to the planner’s ability to adaptively route around noise-induced micro-obstacles, while the energy cost increased by only +0.40%. This quantitative evidence confirms that the favorable accessibility of lower-latitude corridors is not an artifact of resolution smoothing, as the identified pathways remain open and energetically efficient even when error-based roughness is reintroduced.

Furthermore, the analysis reveals a distinct decoupling between instantaneous slope sensitivity and integrated energy consumption. While the high-resolution UN07 target exhibited a significant increase in maximum instantaneous slope (+14.68%) due to artificial pixel-scale roughness generated on the fine 5 m grid, this localized volatility did not propagate to the mission-level energy costs, which remained stable with a bias of less than 1.1% across all targets. This confirms that the noise-induced slope spikes represent traversable micro-texture rather than impassable structural barriers. Consequently, the proposed “Tier I” classification is well-founded, driven by stable macro-topography that persists even under maximum predicted elevation uncertainties.

In addition, we evaluated the impact of terramechanical constraints on energy estimation. Traditional mechanical energy models often underestimate costs in steep terrain by neglecting soil-wheel interactions. By establishing a conservative model that incorporates slope-dependent wheel slip (s) and efficiency losses (η), we observed a non-linear amplification of energy costs. As shown in Supplementary Figure S3, Tier I regions (e.g., UN07) exhibit a narrow cost interval (~24% increase), confirming their high traversability. In contrast, high-slope Tier III regions (e.g., Stose) show a ~47% surge in energy cost and a high uncertainty gap. This widening performance disparity under conservative physical assumptions further reinforces the superiority and robustness of the identified Tier I candidates.

Finally, to contextualize these findings within the broader literature, a direct comparison with the Nobile region routes from Cannon and Britt (2020) confirms topological consistency (see Supplementary Figure S4). While the general corridor locations align, our high-resolution analysis reveals that maximum slopes in these corridors are approximately

23°—significantly steeper than the 16° estimated in the lower-resolution reference study. This 7° discrepancy highlights higher operational risks than previously reported, validating our conclusion that high-resolution data is mandatory for accurate safety assessment.

4.5 Limitations and future work

We acknowledge several limitations in this study that influence the interpretation of our results.

A primary constraint lies in the rover–regolith interaction model, which assumes spatially homogeneous geotechnical parameters derived from mare and highland averages. However, regolith within PSRs is hypothesized to be under-dense and highly porous (potentially exhibiting a “fairy castle” structure) due to the absence of thermal cycling and sintering processes (Hapke, 1993; Gladstone et al., 2012). Such conditions could induce significantly higher wheel sinkage and motion resistance than modeled here; consequently, our reported energy estimates likely represent a conservative lower bound.

Furthermore, our current path planning relies on static average illumination maps. In reality, operational planning is constrained by the dynamic, ephemeral nature of polar lighting. A route that appears geometrically optimal may be thermally or energetically infeasible due to prolonged periods of darkness during the traversal window. However, it is important to note that the geometric flexibility identified in this study (Section 3.2) provides a buffer against this uncertainty: PSRs with multiple accessible corridors (e.g., Tier I targets) are less likely to be fully occluded by transient shadows than those relying on a single trajectory. Future work will aim to integrate time-dependent illumination constraints into the path-planning algorithm to generate 4D (space + time) trajectories that synchronize rover mobility with lighting availability.

Finally, we acknowledge the influence of variable spatial resolution on the comparative analysis. While we utilized the best available LDEMs (Smith et al., 2010; Barker et al., 2021), the resolution varies from 5 m/pixel to 20 m/pixel depending on latitudinal coverage. Coarser resolutions (e.g., 20 m) inherently smooth out high-frequency topography, potentially underestimating the peak slopes and path lengths for targets in these regions. Consequently, the energy estimates for targets derived from 20 m data should be interpreted as a conservative ‘lower bound.’ Targets classified as ‘Tier I’ based on 20 m data may harbor unmapped decameter-scale roughness that would be visible at 5 m resolution, necessitating higher safety margins during actual mission operations.

5 Conclusion

This study provides a comprehensive, quantitative assessment of rover accessibility for 31 priority PSRs at the lunar south pole. By coupling high-resolution topographic data with a terramechanics-based energy model, we have bridged the gap between orbital-scale selection and surface-level mission planning. The key findings and implications are summarized as follows:

First, spatial resolution is a fundamental driver of feasibility. Our comparative analysis reveals that traditional coarser baselines (e.g., 40 m/pixel, as used in previous regional studies such as Cannon and Britt, 2020) smooth over critical hazards. For instance, a direct comparison in the Nobile region (Supplementary Material Section S5) demonstrates that optimal corridors previously estimated at a 16° maximum slope using 40 m/pixel data actually conceal steep 23° peak slopes when accurately resolved at 10 m/pixel. High-resolution path planning demonstrates that for difficult targets (Tier III), safety-optimized trajectories significantly diverge from geometrically shortest paths, incurring higher energy costs to navigate fragmented low-slope corridors.

Second, accessibility is highly non-uniform. We established a three-tier classification framework to guide target prioritization. Tier I targets (e.g., UN11, UN07) exhibit benign terrain with high-margin corridors ($\min(\theta_{max}) < 15^\circ$) and modest energy demands, making them ideal candidates for near-term volatile prospecting. In contrast, Tier III targets (e.g., Shackleton) are guarded by steep crater walls that may exceed the capabilities of conventional wheeled rovers.

Finally, energy constraints challenge current mission architectures. The calculated mechanical energy requirements for deep PSR sorties—particularly when accounting for thermal and communication overheads—suggest that simple “sprint” strategies are unfeasible for many targets. Future mission designs must prioritize energy-efficient routing, “recharge-and-proceed” concepts, and potentially non-solar power solutions for deep interior access.

While limited by the assumption of uniform soil properties and static illumination, these results establish a conservative baseline for identifying operationally viable targets. As the lunar community moves from global mapping to precision landing, this framework provides the physical basis for selecting landing sites that maximize scientific return while minimizing mobility risks.

Data availability statement

The original contributions presented in the study are included in the article/Supplementary Material, further inquiries can be directed to the corresponding author.

Author contributions

YC: Writing – review and editing, Writing – original draft. MY: Data curation, Writing – review and editing. DQ: Supervision, Writing – review and editing. FL: Writing – review and editing.

Funding

The author(s) declared that financial support was received for this work and/or its publication. This work was supported by the National Natural Science Foundation of China (Grant Nos 42595542

and 42030110) and the National Gravitation Laboratory (Grant Nos NGL-2025-018 and NGL-2025-003).

Acknowledgements

We gratefully acknowledge the LRO mission engineers, the LOLA Science Team, and the Diviner Science Team for their relentless efforts in collecting, calibrating, and archiving the data used in this work. We also thank the reviewers for their constructive comments that significantly improved this manuscript.

Conflict of interest

The author(s) declared that this work was conducted in the absence of any commercial or financial relationships that could be construed as a potential conflict of interest.

Generative AI statement

The author(s) declared that generative AI was not used in the creation of this manuscript.

References

- Barker, M. K., Mazarico, E., Neumann, G. A., Smith, D. E., Zuber, M. T., and Head, J. W. (2021). Improved LOLA elevation maps for south pole landing sites: error estimates and their impact on illumination conditions. *Planet. Space Sci.* 203, 105119. doi:10.1016/j.pss.2020.105119
- Barker, M. K., Mazarico, E., Neumann, G. A., Smith, D. E., Zuber, M. T., Head, J. W., et al. (2023). A new view of the lunar south pole from the lunar orbiter laser altimeter (LOLA). *Planet. Sci. J.* 4, 183. doi:10.3847/PSJ/acf3e1
- Bekker, M. G. (1956). *Theory of land locomotion*. Ann Arbor, MI: University of Michigan Press.
- Bekker, M. G. (1969). *Introduction to terrain-vehicle systems*. Ann Arbor, MI: University of Michigan Press.
- Bluethmann, B. (2024). VIPER rover overview and mobility and hardware. *Lunar Surf. Innov. Consort. (LSIC) Technical Presentation. NASA Tech. Rep. Serv.*
- Brown, H. M., Boyd, A. K., Denevi, B. W., Henriksen, M. R., Manheim, M. R., Robinson, M. S., et al. (2022). The resource potential of lunar permanently shadowed regions. *Icarus* 377, 114874. doi:10.1016/j.icarus.2021.114874
- Cannon, K. M., and Britt, D. T. (2020). Accessibility data set for large permanent cold traps at the lunar poles. *Earth Space Sci.* 7, e2020EA001291. doi:10.1029/2020EA001291
- Carrier, W. D. (2003). Particle size distribution of lunar soil. *J. Geotech. Geoenviron. Eng.* 129, 956–959. doi:10.1061/(ASCE)1090-0241(2003)129:10(956)
- Carrier, W. D., Olhoeft, G. R., and Mendell, W. W. (1991). “Physical properties of the lunar surface,” in *Lunar sourcebook: a user's guide to the Moon*. Editors G. H. Heiken, D. T. Vaniman, and B. M. French (Cambridge: Cambridge University Press), 475–594.
- Colaprete, A., Schultz, P., Heldmann, J., Wooden, D., Shirley, M., Ennico, K., et al. (2010). Detection of water in the LCROSS ejecta plume. *Science* 330, 463–468. doi:10.1126/science.1186986
- Dijkstra, E. W. (1959). A note on two problems in connexion with graphs. *Numer. Math.* 1, 269–271. doi:10.1007/BF01386390
- Feldman, W. C., Maurice, S., Binder, A. B., Barraclough, B. L., Elphic, R. C., and Lawrence, D. J. (1998). Fluxes of fast and epithermal neutrons from Lunar Prospector: evidence for water ice at the lunar poles. *Science* 281, 1496–1500. doi:10.1126/science.281.5382.1496
- Gladstone, G. R., Retherford, K. D., Egan, A. F., Kaufmann, D. E., Miles, P. F., Parker, J. W., et al. (2012). Far-ultraviolet reflectance properties of the Moon's permanently shadowed regions. *J. Geophys. Res. Planets* 117, E00H04. doi:10.1029/2011JE003913
- Gläser, P., Scholten, F., De Rosa, D., Figuera, R. M., Oberst, J., Mazarico, E., et al. (2014). Illumination conditions at the lunar south pole using high resolution Digital Terrain Models from LOLA. *Icarus* 243, 78–90. doi:10.1016/j.icarus.2014.08.013
- Hapke, B. (1993). *Theory of reflectance and emittance spectroscopy*. Cambridge University Press.
- Horn, B. K. P. (1981). Hill shading and the reflectance map. *Proc. IEEE* 69, 14–47. doi:10.1109/PROC.1981.11918
- Li, S., Lucey, P. G., Milliken, R. E., Hayne, P. O., Fisher, E., Williams, J. P., et al. (2018). Direct evidence of surface exposed water ice in the lunar polar regions. *Proc. Natl. Acad. Sci. U.S.A.* 115, 8907–8912. doi:10.1073/pnas.1802345115
- Lucey, P. G. (2009). The poles of the Moon. *Elements* 5, 41–46. doi:10.2113/gselements.5.1.41
- Mazarico, E., Neumann, G. A., Smith, D. E., Zuber, M. T., and Torrence, M. H. (2011). Illumination conditions of the lunar polar regions using LOLA topography. *Icarus* 211, 1066–1081. doi:10.1016/j.icarus.2010.10.028
- Mitchell, J. K., Houston, W. N., Carrier, W. D., III, and Costes, N. C. (1974). *Apollo soil mechanics experiment S-200*. Washington, DC: NASA. NASA Contractor Report NASA-CR-134306.
- Mitrofanov, I. G., Sanin, A. B., Boynton, W. V., Chin, G., Garvin, J. B., Golovin, D., et al. (2010). Hydrogen mapping of the lunar south pole using the LRO neutron detector experiment LEND. *Science* 330, 483–486. doi:10.1126/science.1185696
- Nozette, S., Lichtenberg, C. L., Spudis, P., Bonner, R., Ort, W., Malaret, E., et al. (1996). The Clementine bistatic radar experiment. *Science* 274, 1495–1498. doi:10.1126/science.274.5292.1495
- Nozette, S., Spudis, P., Bussey, B., Jensen, R., Raney, K., Winters, H., et al. (2010). The Lunar Reconnaissance Orbiter miniature radio frequency (Mini-RF) technology demonstration. *Space Sci. Rev.* 150, 285–302. doi:10.1007/s11214-009-9607-5
- Paige, D. A., Siegler, M. A., Zhang, J. A., Hayne, P. O., Foote, E. J., Bennett, K. A., et al. (2010a). Diviner lunar radiometer observations of cold traps in the Moon's south polar region. *Science* 330, 479–482. doi:10.1126/science.1187726
- Paige, D. A., Foote, M. C., Greenhagen, B. T., Schofield, J. T., Calcutt, S., Vasavada, A. R., et al. (2010b). The lunar reconnaissance Orbiter diviner lunar radiometer experiment. *Space Sci. Rev.* 150 (1), 125–160. doi:10.1007/s11214-009-9529-2
- Pieters, C. M., Boardman, J., Buratti, B., Chatterjee, A., Clark, R., Glavich, T., et al. (2009). The Moon mineralogy mapper (M³) on Chandrayaan-1. *Curr. Sci.* 96, 500–505.
- Rosenburg, M. A., Aharonson, O., Head, J. W., Kreslavsky, M. A., Mazarico, E., Neumann, G. A., et al. (2011). Global surface slopes and roughness of the Moon from the Lunar Orbiter Laser Altimeter. *J. Geophys. Res. Planets* 116, E02001. doi:10.1029/2010JE003716

Any alternative text (alt text) provided alongside figures in this article has been generated by Frontiers with the support of artificial intelligence and reasonable efforts have been made to ensure accuracy, including review by the authors wherever possible. If you identify any issues, please contact us.

Publisher's note

All claims expressed in this article are solely those of the authors and do not necessarily represent those of their affiliated organizations, or those of the publisher, the editors and the reviewers. Any product that may be evaluated in this article, or claim that may be made by its manufacturer, is not guaranteed or endorsed by the publisher.

Supplementary material

The Supplementary Material for this article can be found online at: <https://www.frontiersin.org/articles/10.3389/fspas.2026.1764826/full#supplementary-material>

- Rubanenko, L., Venkatraman, J., and Paige, D. A. (2019). Thick ice deposits in shallow simple craters on the Moon and Mercury. *Nat. Geosci.* 12 (8), 597–601. doi:10.1038/s41561-019-0405-8
- Sathyan, S., Bhatt, M., Chowdhury, M., Gläser, P., Misra, D., Srivastava, N., et al. (2024). Potential landing sites characterization on lunar south pole: De-Gerlache to Shackleton ridge region. *Icarus* 412, 115988. doi:10.1016/j.icarus.2024.115988
- Siegler, M. A., Miller, R. S., Keane, J. T., Laneuville, M., Paige, D. A., Matsuyama, I., et al. (2016). Lunar true polar wander inferred from polar hydrogen. *Nature* 531, 480–484. doi:10.1038/nature17166
- Smith, D. E., Zuber, M. T., Jackson, G. B., Cavanaugh, J. F., Neumann, G. A., Riris, H., et al. (2010). The lunar Orbiter laser altimeter investigation on the lunar reconnaissance Orbiter mission. *Space Sci. Rev.* 150, 209–241. doi:10.1007/s11214-009-9512-y
- Sowers, G. F., and Dreyer, C. B. (2019). Ice mining in lunar permanently shadowed regions. *New Space* 7, 235–244. doi:10.1089/space.2019.0002
- Speyerer, E. J., and Robinson, M. S. (2013). Persistently illuminated regions at the lunar poles: ideal sites for future exploration. *Icarus* 222, 122–136. doi:10.1016/j.icarus.2012.10.010
- Speyerer, E. J., Lawrence, S. J., Stopar, J. D., Gläser, P., Robinson, M. S., and Jolliff, B. L. (2016). Optimized traverse planning for future polar prospectors based on lunar topography. *Icarus* 273, 337–345. doi:10.1016/j.icarus.2016.03.011
- Spudis, P. D., Nozette, S., Lichtenberg, C., Bonner, R., Ort, W., Malaret, E., et al. (1998). The Clementine bistatic radar experiment: evidence for ice on the Moon. *Sol. Syst. Res.* 32, 17–22.
- Sun, Z. Z., Zhang, T. X., Zhang, H., Jia, Y., Zhang, H. H., Chen, J., et al. (2014). The technical design and achievements of Chang'E-3 probe. *Sci. Sin. Tech.* 44, 331–343. doi:10.1360/N092014-37
- Wang, C., Jia, Y., Xue, C., Lin, Y., Liu, J., Fu, X., et al. (2024). Scientific objectives and payload configuration of the Chang'E-7 mission. *Natl. Sci. Rev.* 11, nwad329. doi:10.1093/nsr/nwad329
- Watson, K., Murray, B. C., and Brown, H. (1961). The behavior of volatiles on the lunar surface. *J. Geophys. Res.* 66, 3033–3045. doi:10.1029/JZ066i009p03033
- Williams, J. P., Greenhagen, B. T., Paige, D. A., Schorghofer, N., Sefton-Nash, E., Hayne, P. O., et al. (2019). Seasonal polar temperatures on the Moon. *J. Geophys. Res. Planets* 124, 2505–2521. doi:10.1029/2019JE006028
- Wong, J. Y., and Reece, A. R. (1967). Prediction of rigid wheel performance based on the analysis of soil-wheel stresses part I. Performance of driven rigid wheels. *J. Terramech.* 4, 81–98. doi:10.1016/0022-4898(67)90105-X
- Zhou, F., Arvidson, R. E., Bennett, K., Trease, B., Lindemann, R., Bellutta, P., et al. (2014). Simulations of Mars rover traverses. *J. Field Robot.* 31, 141–160. doi:10.1002/rob.21483